UC Berkeley
UC Berkeley Previously Published Works

Title

Ice Crystallization During Cold-Start of a Proton-Exchange-Membrane Fuel Cell

Permalink

Journal

ISSN

Authors

Dursch, Thomas J
Liu, Jianfeng F
Trigub, Gregory J
et al.

Publication Date

DOI

Ice Crystallization During Cold-Start of a Proton-Exchange-Membrane Fuel Cell

T. J. Dursch,[1,2] J. F. Liu,[1] G. J. Trigub,[1] C. J. Radke,[1,3] A. Z. Weber[2]

[1] Chemical and Biomolecular Engineering Department, University of California, Berkeley, CA 94720
[2] Environmental Energy Technology Division, Lawrence Berkeley National Laboratory, Berkeley, CA 94720
[3] Earth Sciences Division, Lawrence Berkeley National Laboratory, Berkeley, CA 94720

Under subfreezing conditions, ice forms in the gas-diffusion (GDL) and catalyst layers (CL) of proton-exchange-membrane fuel cells (PEMFCs), drastically reducing cell performance. Although a number of strategies exist to prevent ice formation, there is little fundamental understanding of ice-crystallization mechanisms and kinetics within PEMFC components. We incorporate recently developed ice-crystallization kinetic expressions (1-3) within the CL and GDL of a simplified 1-D transient PEMFC cold-start model. To investigate the importance of ice-crystallization kinetics, we compare liquid-water and ice saturations, and cell-failure time predicted using our kinetic rate expression relative to that predicted using a thermodynamic-based approach. We identify conditions under which ice-crystallization kinetics is critical and elucidate the impact of freezing kinetics on low-temperature PEMFC operation.

Introduction

Proton-exchange-membrane fuel cells (PEMFCs) show promise in automotive application because of their high efficiency, high power density, and potentially low emissions. For automotive applications, PEMFCs must permit rapid startup from sub-freezing temperatures, known as cold-start. In a PEMFC, reduction of oxygen to water occurs in the cathode CL (cCL). Under subfreezing conditions, water solidifies and hinders access of gaseous oxygen to the catalytic sites in the cCL, severely inhibiting cell performance and often causing cell failure (4). Elucidation of the mechanisms and kinetics of ice formation within the cCL is, therefore, critical to successful cell startup and high performance at low temperatures.

Numerous low-temperature PEMFC models have been developed (5-10). Currently, however, no models include ice-crystallization kinetics; consequently, there is no accounting for subcooled liquid (5-10). Models (5-7) commonly assume that product water vapor instantaneously solidifies when the vapor partial pressure exceeds the saturation value. As a result, no liquid water exists within the PEMFC. Recently, Jiao et al. (5) and Balliet et al. (9, 10) extended cold-start models to include vapor, liquid, and solid phases of water within a PEMFC. The freezing points of ice within the catalyst

layer, gas-diffusion layer (GDL), and proton-exchange membrane (PEM) are determined from characteristic pore sizes using the Gibbs-Thomson equation. Although these models include liquid water (8-10), they currently invoke instantaneous thermodynamic freezing and circumvent ice-crystallization kinetics, since at this time, no validated ice-crystallization rate expression exists for a cCL.

Here, we implement our previously developed ice-crystallization kinetic expressions within the cCL and GDL (1-3) in a simplified 1-D transient PEMFC cold-start model. To investigate the importance of ice-crystallization kinetics, we compare liquid-water and ice saturations, and cell-failure time predicted using our kinetic rate expression relative to that predicted using a thermodynamic-based approach (8-10). This exercise allows us to identify conditions under which including ice-crystallization kinetics is critical and to elucidate the impact of freezing kinetics on low-temperature PEMFC performance.

PEMFC Cold-Start Model

Figure 1 illustrates the geometry for a 1-D simplified PEMFC. Dashed lines outline the spatial domain (i.e., we consider only the cCL and cGDL). Symbols a and c label the anode and cathode, respectively. We neglect water transport and subsequent freezing within the anode, since the water diffusion coefficient through the PEM is negligible at subfreezing temperatures (7). Readers are referred to Meng (5), Mao et al. (6, 7), Jiao et al. (8), and Balliet et al. (9, 10) for more detailed 2-D and 3-D cold-start models including thermodynamic ice formation in both the anode and cathode.
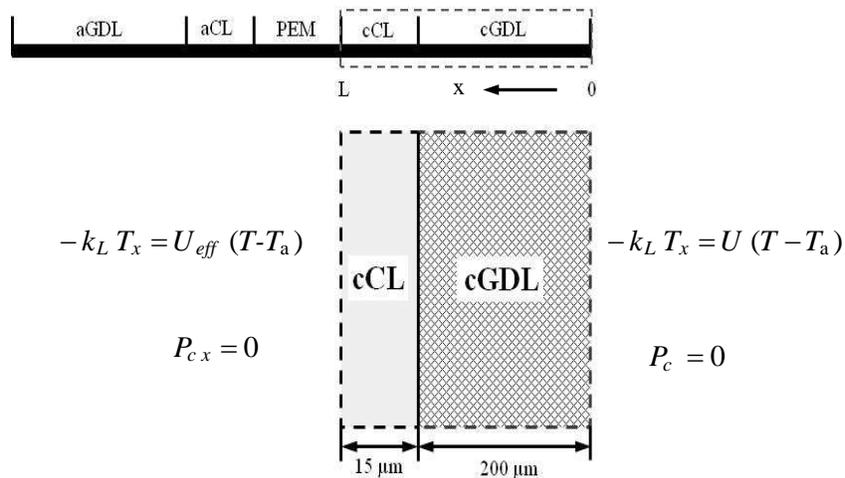
Figure 1. Schematic and boundary conditions for the 1-D PEMFC cold-start geometry. Dashed lines represent the modeling domain. Letters a and c label the anode and cathode, respectively.

Three phases are considered within the cCL and cGDL: gas (G), liquid (L), and ice (I). In each subdomain, phase saturations sum to unity, i.e., $S_G + S_L + S_I = 1$, where the saturation of a phase k, S_k, is defined as volume of phase k per pore volume, $\varepsilon_k / \varepsilon_o$, where ε_o is bulk porosity. Upon thermal equilibrium among all phases (3-7), the 1-D,

transient energy balance to calculate transient temperature distributions, $T(x,t)$, in each subdomain is

$$\overline{\rho \hat{C}_p} \frac{\partial T}{\partial t} = \bar{k}_T \frac{\partial^2 T}{\partial x^2} + \rho_I \varepsilon_o \Delta \hat{H}_f (S_L + S_I) R_I + \dot{Q}_{rxn} \, , \qquad [1]$$

where $\overline{\rho \hat{C}_p}$ is volume-averaged heat capacity, $\bar{k}_T$ is volume-averaged thermal conductivity, $\Delta \hat{H}_f$ is the latent heat of fusion per unit mass of ice (taken as positive), ρ_I is ice mass density, and R_I is the rate of ice formation ((generated ice volume)/(water plus ice volume)/time) (1-3) discussed below. In equation 1, $\dot{Q}_{rxn} = i(\eta_s + \Pi)/L_{cCL}$ in the cCL and zero in the cGDL, where i is volumetric current density, η_s is surface overpotential (calculated from measured isothermal cold-start cell voltage (1)), L_{cCL} is cCL thickness, and Π is the Peltier coefficient (11). The second and third terms on the right side of equation 1 represent enthalpy liberation due to crystallization and reaction, respectively. Because of the low ambient temperatures used in the calculations, heat generation (or consumption) due to evaporation, condensation, sublimation, and deposition (i.e., frosting) are neglected. Additionally, current density in $\dot{Q}_{rxn}$ increases linearly with increasing S_G, so that higher ice and water saturations choke the electrochemical production of liquid water (10). More involved models are discussed elsewhere (8, 10).

In each subdomain, gas-, liquid-, and ice-phase saturations obey the following mass-conservation equations combined with Darcy's law (5-10)

$$\varepsilon_o \rho_G \frac{\partial S_G}{\partial t} = \frac{\partial}{\partial x} \left(\frac{\rho_G k_G [S_G]}{\eta_G} \frac{\partial P_G}{\partial x} \right), \qquad [2]$$

$$\varepsilon_o \rho_L \frac{\partial S_L}{\partial t} = \frac{\partial}{\partial x} \left(\frac{\rho_L k_L [S_L]}{\eta_L} \frac{\partial P_L}{\partial x} \right) - \rho_I \varepsilon_o (S_L + S_I) R_I + R_{rxn} \qquad [3]$$

and

$$\varepsilon_o \rho_I \frac{\partial S_I}{\partial t} = \rho_I \varepsilon_o (S_L + S_I) R_I \qquad [4]$$

where $R_{rxn} = i M_{H_2O}/2F$ in the cCL and R_{rxn} equals zero in the cGDL, η is viscosity, P is pressure, M_{H_2O} is the molar mass of water, and $k_k[S_k]$ is the effective permeability of phase k as a function of S_k. The first, second, and third terms on the right of equation 3 represent water movement due to a gradient in capillary pressure, $P_C \equiv P_G - P_L$, water depletion due to freezing, and water generation due to reaction, respectively. The effective permeabilities in equations 2 and 3 follow the relation $k_k = k_o S_k^3$ (10), where k_o is absolute permeability. Following others (5-10), residual saturations are neglected. To relate capillary pressure, $P_C \equiv P_G - P_L$, to liquid saturation, capillary equilibrium (i.e., Young-Laplace) and a bundle-of-capillaries model are used (12). A detailed description of mixed-wettability for the cCL and cGDL is found in Balliet *et al.* (10).

Equations 1, 3, and 4 contain the ice-crystallization rate, R_I. Under pseudo-isothermal conditions (2), $R_I(\overline{T}_C, \phi)$ is given by

$$R_I(\overline{T}_C, \phi) = k(\overline{T}_C)^{2/5}[1-\phi][-\ln(1-\phi)]^{3/5} \qquad \text{for} \ \ t \geq \overline{\tau}_I, \qquad [5]$$

where $\overline{T}_C$ is number-average crystallization temperature, $\overline{\tau}_I$ is number-average non-isothermal induction time, ϕ is gas-free volume fraction of ice within the pores defined by $\phi \equiv S_I/(S_I + S_L)$. For micro-three-dimensional heat-transfer-limited ice growth, the overall ice-crystallization rate constant, $k(\overline{T}_C)$, in equation 5 is (1)

$$k(\overline{T}_C) = \frac{64\pi}{15} g(\theta) J(\overline{T}_C) \eta_o^3(\overline{T}_C) \alpha_L^{3/2}, \qquad [6]$$

where α_L is liquid thermal diffusivity, $J(T)$ is the pseudo-steady-state nucleation rate, $\eta_o(T)$ is a dimensionless temperature-dependent growth parameter (see equation 9 of (1)), θ is the contact angle of the ice/water/substrate triple line, and $g(\theta) = (2+\cos\theta)(1-\cos\theta)^2/4$, for heterogeneous nucleus growth on a flat surface. Equation 5 applies only for $t > \overline{\tau}_I$. Following our previous approach (2), $\overline{\tau}_I$ is given by

$$\int_0^{\overline{\tau}_I} \frac{dt}{\overline{\tau}_i(T)} = 1, \qquad [7]$$

where $\overline{\tau}_i(T)$ is number-average isothermal induction time, given by $\overline{\tau}_i(T) = 1/J(T)V_o$ (1), where V_o is initial liquid volume in either the cCL or cGDL. Detailed discussion of the ice-crystallization kinetic parameters is found in Dursch *et al.* (1-3).

Coupled, nonlinear partial-differential equations 1-7 are solved simultaneously subject to the boundary conditions provided in Figure 1. In all cases here, initial liquid-water and gas pressures are uniformly 101.3 kPa, corresponding to initial liquid-water saturations, S_{Lo}, of 0.34 and 0.22 in the cCL and cGDL, respectively. Initial temperature is uniform at the ambient subcooling, $\Delta T = 273.15 - T_a$, where T_a is the ambient temperature. Equations are solved numerically in Matlab R2010a (The Math Works Inc., Natick, MA) using central finite differencing and Crank-Nicholson iteration to resolve nonlinearities with a tolerance of 10^{-7}, a time step of 10^{-2} s, and 50 mesh elements. The inversion scheme BAND(j) solves the resulting tridiagonal matrices (13). All model parameters are listed in Table I.

Table I. Model Parameters

Parameter	cCL	cGDL
ε_o	0.5	0.8
$\overline{\rho \hat{C}_p}$ (kJ m^{-3} K^{-1})	990	970
$\bar{k}_T$ (W m^{-1} K^{-1})	1.2	1.5
k_o (m^{-2})	1×10^{-15}	1×10^{-12}
η_s (V)	0.55	–
Π (V)	-0.012	–
U (W m^{-2} K^{-1})	100	90
A (nuclei m^{-3} s^{1})	1.1×10^{10}	9.1×10^{7}
B (K^{3})	4.0×10^{5}	1.1×10^{5}

Results and Discussion

Figure 2 displays typical calculated liquid-water saturations, S_L, as a function of time, t, at the coldest boundaries of the cCL ($x = L$) and cGDL ($x = 0$) at equal subcoolings, ΔT, of 10 K at $x = 0, L$ and $i = 40$ mA/cm^2. Solid lines reflect the proposed ice-crystallization kinetic model in equations 5-7. Initially, S_L increases in both the cCL and cGDL as a result of water generation in the cCL and subsequent migration to the cGDL due to a gradient in capillary pressure. S_L continues to increase until crystallization first commences in the cGDL at the number-average non-isothermal induction time, $\bar{\tau}_I$, where liquid water rapidly transforms into ice (1-3). In the cCL, $\bar{\tau}_I$ is considerably longer than that in the cGDL due to slower ice nucleation rates (1, 3). Consequently, S_L increases over a longer time period prior to freezing. S_L and T profiles at given times are omitted, as both are essentially uniform spatially due to a small Biot number ($Bi = 0.002$) and a fast time-scale for water movement.

Conversely, dashed and dotted lines in Figure 2 are calculated using a thermodynamic-based approach (9), where the ice-formation rate is proportional to the liquid-water saturation by a freezing rate constant, $R_I \approx k_f S_L$ (equation 14 in (9)). Dashed and dotted lines correspond to $k_f = 0.25$ and 1 kg/m^{3}s, respectively (9). In this approach, freezing begins once the local temperature is less than the equilibrium freezing temperature, T_o. At $\Delta T = 10$ K, T_a is well below T_o in the cCL (270.2 to 271.1 K (14)) and in the cGDL (273.0 K (14)). Accordingly, S_L decreases abruptly in both cases due to immediate freezing. Figure 2 highlights the importance of $\bar{\tau}_I$ in the cCL for forestalling freezing.
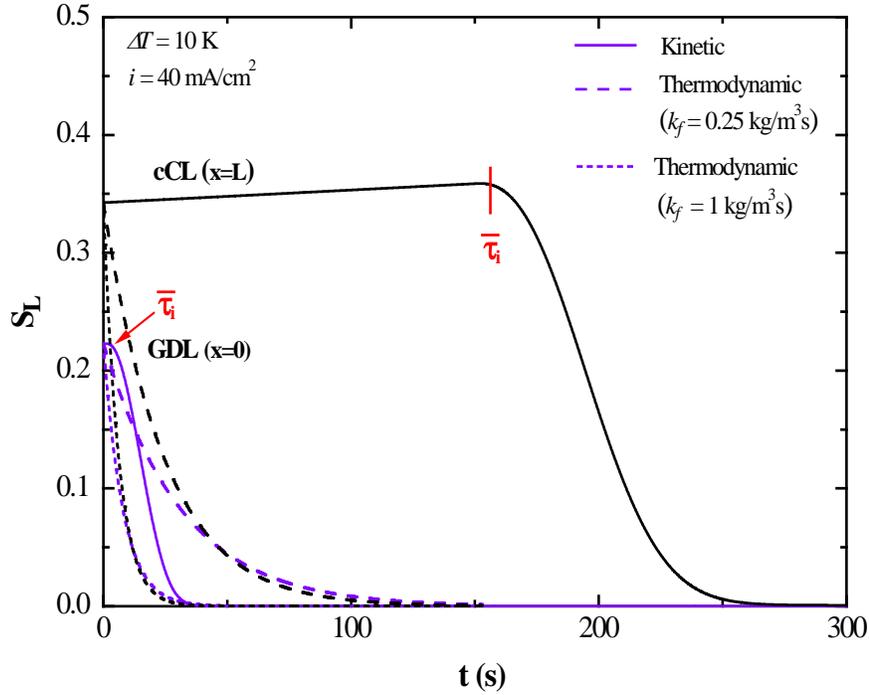
Figure 2. Calculated liquid-water saturation, S_L, as a function of time, t, at the coldest boundary of the cCL ($x = L$) and cGDL ($x = 0$) for a subcooling, ΔT, of 10 K. Solid lines are calculated using ice-crystallization kinetics, equations 5-7. Dashed and dotted lines are predicted assuming thermodynamic equilibrium with $k_f = 0.25$ and 1 kg/m^{3}s, respectively (9). $\bar{\tau}_I$ labels the number-average non-isothermal induction times for the cCL and the cGDL.

The likelihood of successful cold-start depends strongly on temperature through $\bar{\tau}_I$. Thus, to elucidate those conditions for which including ice-crystallization kinetics is critical, we examine isothermal cell-failure time, t_{fail}, for varying subcoolings, ΔT (i.e., ambient temperatures). In this work, we define t_{fail} as the time for which ice saturation reaches 0.38 in either the cCL or the cGDL, thereby choking the cell. $S_{Ifail} = 0.38$ was obtained from a fit of experimental cell voltage versus time at $\Delta T = 10$ K and $i = 40$ mA/cm^2 (4). Upon cell failure, a partially-ice-saturated cCL (i.e., $S_{Ifail} < 1$) is consistent with experimental observation, especially for low subcoolings (4).

Figure 3 displays t_{fail} as a function of ΔT for an isothermal galvanostatic cold-start. Solid lines correspond to ice-crystallization kinetics from equations 5-7 for two cCL carbon-support materials with considerably different ice-crystallization kinetics (i.e., Vulcan XC72 and Black Pearls 460 (3)). The dashed line is calculated using the thermodynamic-based expression with $k_f = 0.25$ kg/m^{3}s (9). In all cases, t_{fail} decreases substantially with increasing ΔT, in good agreement with experiment (4). In both the kinetic and thermodynamic approaches, t_{fail} decreases to a limiting value of 0.1 h. Accordingly, two limiting regimes for t_{fail} are evident in Figure 3. For small subcoolings (i.e., $\Delta T < 3$ K and $\Delta T < 11$ K for thermodynamic and kinetic freezing, respectively),

t_{fail} is limited by freezing, whereas for larger subcoolings, t_{fail} is limited water production (e.g., see Figure 2 for the latter case).
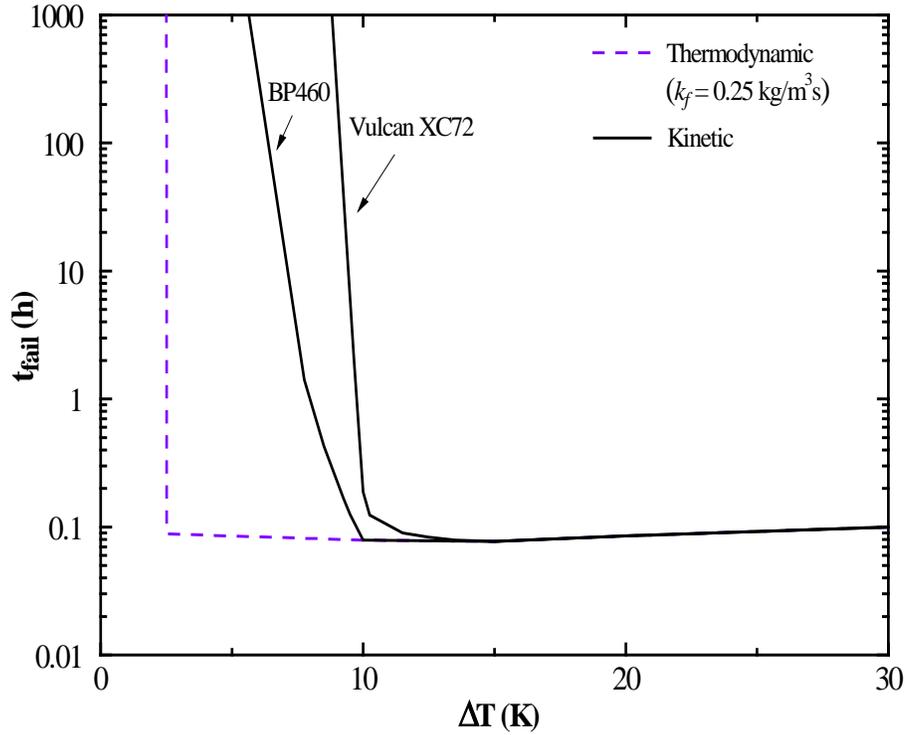
Figure 3. Cell-failure time, t_{fail}, for isothermal galvanostatic start-up as a function of subcooling, ΔT. Solid lines are calculated using ice-crystallization kinetics in the BP460 and Vulcan XC72 cCLs. The dashed line is calculated using a typical thermodynamic-based rate expression (9).

In both the cCL and cGDL, $\bar{\tau}_I$ decreases significantly at lower subcoolings (1-3). Consequently, as subcooling extends beyond $\Delta T = 11$ K, $\bar{\tau}_I$ is negligible in both cell domains, and ice-crystallization kinetics is well approximated by the thermodynamic-based approach. We conclude that including ice-crystallization kinetics is critical in the "nucleation-limited" regime (see Figure 14 of (1)) where induction times are long (i.e., from $3 \leq \Delta T \leq 10$ K in Figure 3). However, the particular ΔT that establishes the "nucleation-limited" regime relies heavily on all heat transfer and kinetic parameters (e.g., U, U_{eff}, $\bar{k}_T$, and $J(T)$). These controlling parameters can be adjusted to lengthen $\bar{\tau}_I$, significantly delaying or even preventing ice formation.

As an example, Figure 4 displays ice saturations, S_I, as a function of time, t, at the coldest boundaries of the cCL ($x = L$) and cGDL ($x = 0$) at equal subcoolings, ΔT, of 10 K at $x = 0, L$ and $i = 40$ mA/cm^2 with varying overall heat transfer coefficient U and fixed U_{eff}. Lines are calculated using $U = 100$ and 15 W/m^2 K (dashed). Clearly, S_I decreases to zero in both the cCL and cGDL as U decreases from 100 to 15 W/m^2 K, even for a subcooling of 10 K. This result demonstrates that decreasing U (i.e., increasing thermal insulation) forestalls or even eliminates call failure upon cold-start because heat generated by reaction now prevents freezing.
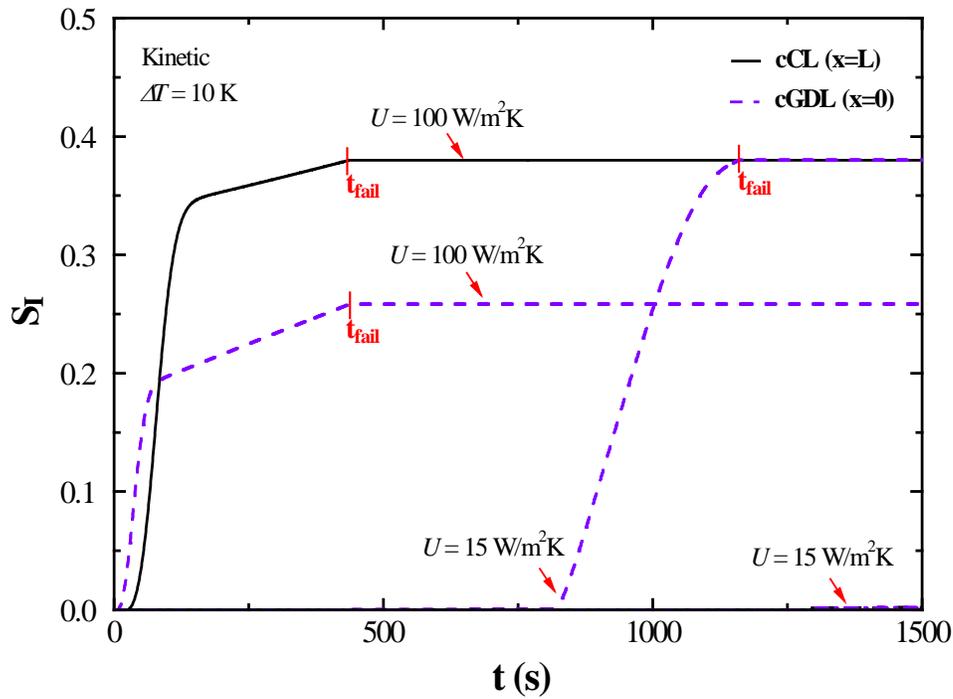
Figure 4. Calculated ice saturation, S_I, as a function of time, t, at the coldest boundaries of the cCL ($x = L$) and cGDL ($x = 0$) for a subcooling, ΔT, of 10 K. Lines are calculated using ice-crystallization kinetics, equations 5-7, with $U = 100$ and 15 W/m^2 K. Solid lines correspond to the cCL, whereas dashed lines correspond to the cGDL. The symbol t_{fail} denotes the cell-failure time.

Summary

In this study, we incorporate our previously developed ice-crystallization kinetic expressions within the cCL and cGDL of a simplified 1-D transient PEMFC cold-start model. To investigate the importance of ice-crystallization kinetics, we compare liquid-water and ice saturations, and cell-failure times predicted using our kinetic rate expression relative to that predicted using a thermodynamic-based approach. Significantly, the simplified cold-start model illustrates that ice-crystallization kinetics is critical in the "nucleation-limited" regime where induction times are long (i.e., corresponding to small subcoolings and/or low overall heat transfer coefficients).

References

1. T.J. Dursch, M.A. Ciontea, C.J. Radke, and A.Z. Weber, *Langmuir*, **28**, 1222 (2012).
2. T.J. Dursch, M.A. Ciontea, G.J. Trigub, C.J. Radke, and A.Z. Weber, *J. Heat and Mass Transfer*, **60**, 450 (2013).
3. T.J. Dursch, M.A. Ciontea, G.J. Trigub, C.J. Radke, and A.Z. Weber, *ECS Trans.*, **50**, 429 (2012).
4. C. Chacko, R. Ramasamy, S. Kim, M. Khandelwal, M. Mench, *J. Electrochem. Soc.*, **155**, B1145 (2008).
5. H. Meng, *J. Power Sources*, **178**, 141 (2008).
6. L. Mao, C.Y. Wang, Y. Tabuchi, *J. Electrochem. Soc.*, **154**, B341 (2007).
7. L. Mao, C.Y. Wang, *J. Electrochem. Soc.*, **154**, B139 (2007).
8. K. Jiao, X. Li, *Electrochim.* Acta, **54**, 6876 (2009).
9. R. Balliet, K.E. Thomas-Alyea, J. Newman, *ECS Trans.*, **16**, 285 (2008).
10. R. Balliet, J. Newman, *J. Electrochem. Soc.*, **158**, B927 (2011).
11. A.Z. Weber, J. Newman, *Chem. Rev.*, **104**, 4679 (2004).
12. A.Z. Weber, *J. Power Sources*, **195**, 5292 (2010).
13. J. Newman, K.E. Thomas-Alyea, Electrochemical Systems, third ed., John Wiley & Sons, New Jersey, 2004, pp. 30-40.
14. Y. Ishikawa, T. Morita, K. Nakata, K. Yoshida, M. Shiozawa, *J. Power Sources*, **163**, 708 (2007).